Journal of Power Sources 285 (2015) 449–459

Contents lists available at ScienceDirect

Journal of Power Sources

journal homepage: www.elsevier.com/locate/jpowsour

Effect of different processes and Ti/Zn molar ratios on the structure, morphology, and enhanced photoelectrochemical and photocatalytic performance of Ti^{3+} self-doped titanium–zinc hybrid oxides

Rongrong Fu [a], Qingyao Wang [a], Shanmin Gao [a, b, **], Zeyan Wang [b], Baibiao Huang [b], Ying Dai [b], Jun Lu [c, *]

[a] College of Chemistry and Materials Science, Ludong University, Yantai 264025, China
[b] State Key Laboratory of Crystal Materials, Shandong University, Jinan 250100, China
[c] Chemical Sciences and Engineering Division, Argonne National Laboratory, Argonne, IL 60439, USA

HIGHLIGHTS

- Ti^{3+} self-doped titanium–zinc hybrid oxides heterojunctions were synthesized.
- The Ti^{3+} enhanced the photoabsorption and increased the electron transfer rate.
- The heterojunctions exhibits excellent photocurrent and photocatalytic activity.
- A synergetic effect of photocatalysis in the photocatalytic process.

GRAPHICAL ABSTRACT

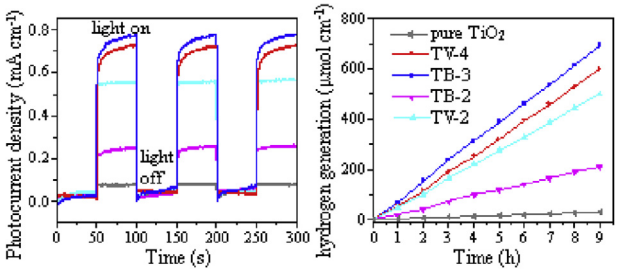

ARTICLE INFO

Article history:
Received 2 January 2015
Received in revised form
22 February 2015
Accepted 11 March 2015
Available online 12 March 2015

Keywords:
Ti^{3+} self-doped
Hybrid oxides
Heterojunction
Hydrogen production
Visible light photocatalyst

ABSTRACT

Ti^{3+} self-doped titanium–zinc hybrid oxides with different phase compositions and morphologies were successfully synthesized using Zn powder as the reductant and Zn source by a chemical-reduction precipitation method with subsequent thermal treatment. The fabricated Ti^{3+} self-doped TiO_2(A)/TiO_2(R), TiO_2(A)/TiO_2(R)/$ZnTiO_3$, and TiO_2(A)/ZnO heterojunctions were characterized by X-ray diffraction, transmission electron microscopy, high-resolution transmission electron microscopy, X-ray photoelectron spectroscopy, and UV–Vis diffuse reflectance spectroscopy. The effects of various Ti/Zn molar ratios and preparation processes on the structural, morphological, optical, photocurrent and photocatalytic properties of the resultant samples were investigated systematically. Results reveal that Ti^{3+} self-doping enhances the photoabsorption capability of titanium–zinc hybrid oxides in the visible-light region. Moreover, different processes and Ti/Zn molar ratios play great influences on the structure, morphology, optical, photocurrent and photocatalytic properties of the final products. Ti^{3+} self-doped titanium–zinc hybrid oxides exhibit excellent photocurrent and photocatalytic activity than pure TiO_2 and $ZnTiO_3$ under visible-light irradiation ($\lambda \geq 400$ nm). The most active Ti^{3+} self-doped titanium–zinc hybrid oxides photoanode presents significantly improved water splitting performance. The synergistic effect between the Ti^{3+} self-doped and heterojunctions is responsible for the enhanced performance of these materials.

Published by Elsevier B.V.

1. Introduction

Photocatalysis has been continuously developed as a promising alternative technology for water splitting and environmental

* Corresponding author.
** Corresponding author. College of Chemistry and Materials Science, Ludong University, Yantai 264025, China.
E-mail addresses: gaosm@ustc.edu (S. Gao), junlu@anl.gov (J. Lu).

http://dx.doi.org/10.1016/j.jpowsour.2015.03.070
0378-7753/Published by Elsevier B.V.

purification. As photocatalytic materials, TiO_2 and ZnO are technologically important because of their versatile applications in decontamination of polluted water, hydrogen generation, solar cell, pigments, and UV shielding materials, etc [1]. Photocatalytic activity is well known to be strongly related to physical properties, such as crystal phase, particle size, crystallinity, and morphology [2,3]. Various tailored morphologies, such as nanorods, nanotubes, and nanoflakes, have been observed to perform an important function in achieving fast charge transfer and efficient charge separation to achieve improvements in photocatalytic activity [4–6]. By selecting different preparation methods and controlling synthesis conditions, TiO_2 and ZnO can be easily used to form various types of nanostructures for applications in photocatalysis or solar cell [7].

However, major drawbacks, such as wide band gaps (anatase TiO_2 (TiO_2(A)) and ZnO, 3.2 eV; rutile TiO_2 (TiO_2(R)), 3.0 eV) and poor quantum yields caused by rapid recombination of photoinduced electrons and holes, impede the practical applications of pristine TiO_2 and ZnO-based photocatalytic oxidation. Only UV light can be utilized to generate electron–hole pairs and initiate the photocatalytic oxidation process. Thus, enhancing the light harvesting and quantum efficiency of TiO_2 and ZnO photocatalysts is a worthwhile endeavor [1].

An effective method to control the recombination of photoinduced electrons and holes is to form heterojunction structure between TiO_2 and ZnO with similar band gaps and staggered band positions. Such a heterojunctions will increase the electron–hole separation, prolong charge lives, extend the photoresponsive range, and increase photocatalytic efficiency [8–11]. The superior photocatalytic activity of bicomponent semiconductors containing titania and zinc is attributed to a decrease in the electron–hole pair recombination rate and an increase in lifespan [12,13]. Fundamental studies on the phase and characterization of TiO_2–ZnO systems have been conducted, and five compounds have been observed to exist in this binary system, including $ZnTiO_3$ (cubic, hexagonal), Zn_2TiO_4 (cubic, tetragonal), and $Zn_2Ti_3O_8$ (cubic) [14,15]. Recent studies have shown that the hexagonal phase $ZnTiO_3$ can be used as a photocatalyst [15,16]. However, similar to pure TiO_2 and ZnO, $ZnTiO_3$ is a wide-band gap semiconductor that cannot be activated by visible light [15]. In order to expand the absorption of $ZnTiO_3$ to the visible-light region or improve the photocatalytic efficiency, the metal-doped $ZnTiO_3$ or $ZnTiO_3$/TiO_2 heterojunction structure were reported [17,18]. Surendar et al. [17] have prepared La-doped $ZnTiO_3$ nanoparticles and studied their photocatalytic activity, which indicated that the sample with a cubic phase showed the best catalytic performance. Cai et al. synthesized $ZnTi_3$/TiO_2 heterojunction structure with $ZnTiO_3$ nanosheets and TiO_2 tubular array. However, the process is rather complicated with the additional utilization of laser ablation [18].

Self-doped TiO_2 and ZnO, which contain an oxygen vacancy (Ov), have recently been reported to exhibit significant photocatalytic activity in the visible-light region [19,20]. Compared with conventional doping methods, Ov is a type of self-doping that does not introduce impure elements into the material, which is favorable for preserving the intrinsic crystal structures and high stability of TiO_2 or ZnO during the visible light photocatalytic progress. A significant amount of research has been focused on the relationship between the oxygen defects and photocatalytic activity of TiO_2 and ZnO [21–24]. For TiO_2, the Ov can form a localized state under the conduction band edge of TiO_2; while, for ZnO, the Ov can form a localized state above the valence band edge. When the concentration of Ov is increased, the impurity states become more delocalized and overlap with the CB or VB edge, resulting in the band gap narrowing. This makes the self-doped TiO_2 and ZnO absorb visible light. Thus, evaluating facile synthetic methodologies for self-doped TiO_2 and ZnO with active visible-light response is particularly recommended [25].

Based on the results of past investigations, we introduce a simple method to prepare Ti^{3+} self-doped titanium–zinc hybrid oxides. In our previous work, we reported a hydrothermal process for synthesizing Ti^{3+} self-doped TiO_2(A)/TiO_2(R) heterojunctions using Zn powder as the reductant [26]. Heterojunction architectures and Ti^{3+} contents may be controlled by adjusting the temperature of hydrothermal treatment. In this study, we used $Ti(SO_4)_2$ as a Ti source and zinc powder as a reducing agent and Zn source, Ti^{3+} self-doped titanium–zinc hybrid oxides were prepared through heat treatment of the solid precursors obtained from different stages during the preparation process. The effects of Ti/Zn molar ratios and preparation processes on the structure, morphology, composition, photoelectrochemical and photocatalytic performance in visible light were studied in detail. The formation of TiO_2(A)/TiO_2(R), TiO_2(A)/TiO_2(R)/$ZnTiO_3$ or TiO_2(A)/ZnO heterojunctions improved the separation efficiency of the charge carriers, which improved photoelectrochemical and photocatalytic activities for water splitting and photocatalytic degradation of RhB under visible-light irradiation. The formation and photocatalytic mechanisms of Ti^{3+} self-doped titanium–zinc hybrid oxides were investigated. The novel system proposed in this work presents potential advantages of enhanced or tunable sunlight absorption, improved photogenerated electron–hole separation, and efficient charge transfer.

2. Experimental

2.1. Sample preparation

$Ti(SO_4)_2$, Zn powder, and NaOH were of reagent grade, obtained from Ruijinte Chemical Reagent Co. (Tianjin, China), and used without further purification. Double distilled water was used throughout the experiments. In a typical procedure, 2.40 g of $Ti(SO_4)_2$ powder was dissolved in 40 mL of deionized water. Subsequently, Zn powder was added to the $Ti(SO_4)_2$ solution at different molar ratios under vigorous stirring. The suspension was continuously stirred for 30 min at room temperature and then filtered to yield a black precipitate and clear bluish violet solution. Following filtration, 0.6 mol/L NaOH was added to the resultant solution to adjust the pH to 5,6 and formed a bluish violet precipitate. The black and bluish violet precipitates obtained were dried at 80 °C in vacuum. Further heat treatment was conducted at 550 °C for 3 h under a nitrogen atmosphere. The heating rate was 5 °C min^{-1} and the flow rate of nitrogen was 10 mL min^{-1}. Samples with different amounts of Zn powder were prepared under identical conditions to investigate the effect of the amount of Zn powder on the structure, morphology, and photocatalytic properties of Ti^{3+} self-doped titanium–zinc hybrid oxides. For convenience, samples obtained from the black and bluish violet precipitates were designated as TB-x and TV-x, respectively, where -x indicates the molar ratio of Ti/Zn. For comparison, pure TiO_2 and $ZnTiO_3$ were prepared according to the literature [15].

2.2. Characterization

The phases of the final products were identified using an X-ray diffractometer (XRD; Rigaku D/max-2500VPC) with Ni-filtered Cu-Kα radiation (λ = 1.5418 Å) from $2\theta = 20°–80°$ with a scan rate of 0.02°/s. Transmission electron microscopy (TEM) and high-resolution transmission electron microscopy (HRTEM) measurements were carried out on a JEOL-2100 microscope. X-ray photoelectron spectra (XPS) measurements were performed on an X-ray photoelectron spectrometer (VG Micro Tech ESCA 3000) using

monochromatic Al-Kα with photon energy of 1486.6 eV and a reference C1s peak of 284.6 eV. UV–Vis diffuse reflectance spectra (DRS) were recorded on a Shimadzu UV-2550 UV–Vis spectrophotometer at room temperature from 200 nm to 800 nm, in which fine $BaSO_4$ was used as the reflectance standard.

2.3. Photoelectrode preparation

Ti^{3+} self-doped titanium–zinc hybrid oxides, pure TiO_2, and $ZnTiO_3$ photoelectrodes were prepared by spreading aqueous slurry of the samples over 1.0 cm^2 of FTO (F-doped SnO_2) glass substrates. A suspension of 2.5 g/L samples was prepared in ethanol by ultrasonication for more than 30 min. A 25 μL suspension was then printed onto an FTO conductive glass substrate through a screen mesh to form a transparent film. All samples were dried in an oven at 120 °C for 30 min and then annealed at 300 °C for 2 h.

2.4. Photocatalytic activity measurements

The photocatalytic performances of the as-prepared samples were evaluated by the degradation of RhB dyes. A Xe lamp (power, 300 W; PLS-SXE300, Beijing Trusttech Co., Ltd., China) equipped with a UV cutoff filter was used as a light source to provide visible light ($\lambda \geq 400$ nm). The visible light illumination intensity is 80 mW cm^{-2}. During the degradation of RhB dye, a total sample mass of 0.04 g was added to 100 mL RhB aqueous solution (concentration, 5.0×10^{-4} M) in a customized quartz reactor. The concentration of RhB was monitored by UV–Vis spectroscopy. Each suspension was magnetically stirred in the dark for 30 min to obtain a good dispersion and reach an adsorption–desorption equilibrium between RhB and the photocatalysts; the suspensions were then irradiated by visible light. After 10 min intervals during visible-light illumination, about 3 mL aliquots were taken out and centrifuged to remove the trace particles. The absorbance of the centrifuged solution was measured from 200 nm to 800 nm using a UV–Vis spectrophotometer (Shimadzu UV-2550). During the photoreactions, no oxygen was bubbled into the suspension. Similar measurements were also performed on the pure TiO_2 and $ZnTiO_3$ for comparative purposes.

Active species capture and hydroxyl radical (•OH) testing experiments were conducted to study the photocatalytic mechanism of the oxide products and detect active species during photocatalytic reactivity in detail. The experimental procedure is similar to photocatalysis. For active species capture experiments, 1.0 mM *tert*-butanol (TBA, a quencher of •OH), ammonium oxalate (AO, a quencher of h^+), and *p*-benzoquinone (BQ, a quencher of $\bullet O_2^-$) solution were added to RhB solution. For •OH testing experiments, the aqueous solution of RhB was replaced by 5×10^{-4} M terephthalic acid (TA) solution with 2×10^{-3} M NaOH. Following 10 min of irradiation, 2.0 mL of the solution was obtained, centrifuged, and subjected to fluorescence spectroscopy using a PerkinElmer LS 55 fluorescence spectrometer. An excitation light wavelength of 320 nm was used to record fluorescence spectra. No oxygen was bubbled into the suspension during the photoreactions.

2.5. Photoelectrochemical and hydrogen evolution measurements

Photocurrent was measured on a standard three-electrode cell using a CHI 600E potentiostat/galvanostat (Shanghai Chenhua Instrumental Co., Ltd., China). The as-prepared photoelectrodes were used as working electrode; the Pt wire and a saturated calomel electrode (SCE) were worked as counter electrode and reference electrodes, respectively. A 0.25 M Na_2S and 0.35 M Na_2SO_3 aqueous solution was used as electrolyte. The visible-light source was the same as the photocatalytic process. The amount of H_2 evolved was determined with a gas chromatograph (Techcomp-GC7890-II, nitrogen as a carrier gas), which connected to a circulation line and equipped with thermal conductivity detector (TCD).

3. Results and discussion

3.1. Characterization of the samples

The Ti^{3+} self-doping enhances the photoabsorption capability of titanium–zinc hybrid oxides in the visible-light region. Moreover, the Ti/Zn molar ratio is a key factor that has significant impact on the structure, morphology, and composition of the products. The crystalline structures of samples obtained using different processes and Ti/Zn molar ratios were determined by X-ray diffraction (XRD). The average crystallite sizes of the samples were estimated by using the Debye–Sherrer formula. The XRD results (Fig. 1) reveal that the different processes and Ti/Zn molar ratios significantly influenced the phase transformation and composition of the products. At a high molar ratio of Ti/Zn, the sample from the black precipitate was pure anatase TiO_2 (Fig. 1; TB-4) and the sample from the bluish violet precipitate was a mixture of anatase and rutile TiO_2 (Fig. 1; TV-4). The peaks at $2\theta = 25.3°$, 37.9°, 48.1°, 54.1°, 55.1°, 62.7°, 68.8°, 70.3° and 75.0° were indexed to (101), (004), (200), (105), (211), (204), (116), (220) and (215) crystal planes of anatase TiO_2 (JCPDS Card No. 21-1272); the peaks at $2\theta = 27.5°$, 36.0°, 41.3°, 54.4°, 56.4° and 69.0° were assigned to (110), (101), (111), (211), (220) and (301) crystal planes of rutile TiO_2 (JCPDS Card No. 21-1276), respectively. The average crystallite sizes of the TiO_2(A) and TiO_2(R) were 7 nm and 15 nm, respectively, based on the TiO_2(A) peak (101) and TiO_2(R) peak (101). When the molar ratio of Ti/Zn was 3, the sample obtained from the black precipitate was primarily composed of a mixture of anatase and rutile TiO_2, although traces of other products were also observed (Fig. 1; TB-3). Peaks at $2\theta = 32.7°$ and 35.4° were indexed to the (104) and (110) crystal planes of hexagonal-phase $ZnTiO_3$ (JCPDS Card No. 26-1500), respectively. By contrast, the sample obtained from the bluish violet precipitate was primarily composed of hexagonal-phase $ZnTiO_3$ and a small quantity

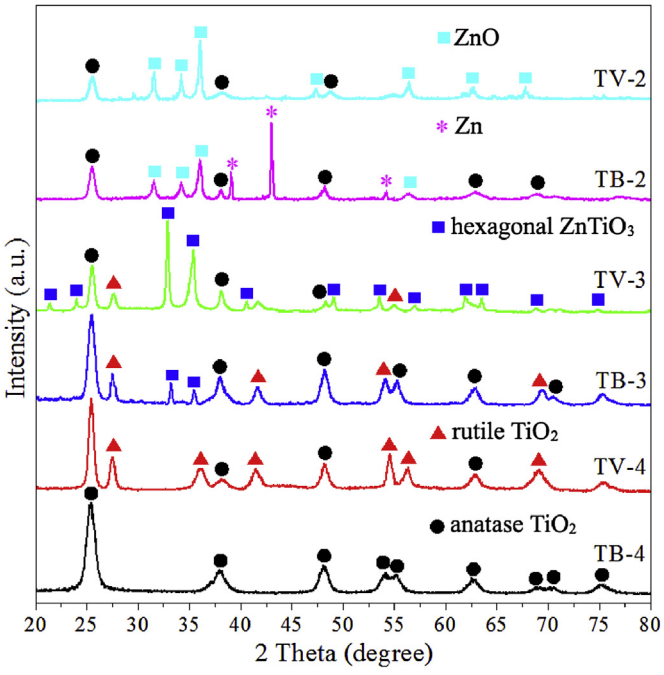

Fig. 1. XRD patterns of the samples obtained at different process and Ti/Zn molar ratio.

of TiO_2 (Fig. 1; TV-3). The peaks at $2\theta = 21.3°$, 24.0°, 32.8°, 35.4°, 40.5°, 48.9°, 53.5°, 56.9°, 61.8°, 63.4°, 68.7° and 74.7° were indexed to (101), (012), (104), (110), (113), (024), (116), (018), (214), (300), (208) and (220) crystal planes of hexagonal phase $ZnTiO_3$ (JCPDS Card No. 26-1500), respectively. The $ZnTiO_3$ average crystallite size of the sample TV-3 is 17 nm that was estimated from the (104) peak. Based on a ZnO–TiO_2 phase diagram previously obtained [27], hexagonal-phase $ZnTiO_3$ forms at approximately 700 °C. Kong et al. determined that pure hexagonal-phase $ZnTiO_3$ can be achieved at 800 °C for 3 h and that this product exhibit high photocatalytic activity under solar light irradiation [15]. However, we obtained hexagonal-phase $ZnTiO_3$ at 550 °C for 3 h; here, the heat treatment temperature is lower by approximately 200 °C than that reported in the literature. When the molar ratio of Ti/Zn reached 2:1, the product obtained from the black precipitate included TiO_2 and ZnO; but there is a small amount of incomplete reaction of the Zn powder (Fig. 1; TB-2). Peaks at $2\theta = 38.9°$, 43.1°, and 54.2° were indexed to the (100), (101), and (102) crystal planes of Zn (JCPDS Card No. 65-5973). The peaks at $2\theta = 31.5°$, 34.3°, 36.1° and 56.5° were indexed to (100), (002), (101) and (110) crystal planes of zincite ZnO (JCPDS Card No. 36-1451). The product from the bluish violet precipitate contained anatase TiO_2 and zincite ZnO only (Fig. 1; TV-2). The average crystallite sizes of the ZnO is about 23 nm (based on the (101) peak of ZnO).

As XRD analysis indicated that Ti/Zn molar ratios and precipitates obtained from different precipitation processes affect the composition of the final products, we assumed that these factors may also affect the product morphologies. Our hypothesis was confirmed by the sample microstructures obtained via transmission electron microscopy (TEM) and high-resolution transmission electron microscopy (HRTEM).

Fig. 2 shows the TEM and HRTEM images of the samples obtained from different precipitation processes and Ti/Zn molar ratios. When the molar ratio of Ti/Zn was 4:1, the sample from the black precipitate consisted of slight aggregates particles (Fig. 2a, TB-4). The morphology of the sample obtained from the bluish violet precipitate grew regularly and comprised nanoparticles and some nanorods (Fig. 2b, TV-4). The corresponding HRTEM image (Fig. 2c) displayed two types of clear lattice fringes. One set of the fringes spacing was ca. 0.35 nm, corresponding to the (101) plane of TiO_2(A). The distance between the lattice fringes of 0.32 nm in the nanorods was ascribed to the interplanar distance of the (110) plane of TiO_2(R). The HRTEM result was consistent with the XRD results that indicated the formation of TiO_2(A)/TiO_2(R) heterojunctions for sample TV-4 [26]. When the molar ratio of Ti/Zn was 3, the sample from the black precipitate was made of a large number of nanoparticles and a small quantity of nanorods and small nanoflakes (Fig. 2d, TB-3). The sample obtained from the bluish violet precipitate comprised many thin nanoflakes and a small amount of nanoparticles attached to the nanoflake surfaces (Fig. 2e, TV-3). Fig. 2f is the HRTEM image of the sample TV-3. The fringes spacing was about 0.27 nm, corresponding to the (104) plane of hexagonal $ZnTiO_3$. Based on the XRD and HRTEM results, it can be concluded that the nanoparticles and nanorods are in the anatase and rutile TiO_2 phases and that the nanoflakes are hexagonal-phase $ZnTiO_3$. These results also indicated that the TiO_2(A)/TiO_2(R)/$ZnTiO_3$ heterojunctions were formed when the molar ratio of Ti/Zn was 3. Sample TB-2 was composed of regular spherical nanoparticles with slight aggregation between nanoparticles (Fig. 2g). The morphology of sample TV-2 grew irregularly and comprised nanoparticles and nanoflakes (Fig. 2h). HRTEM image in Fig. 2i displays two types of lattice fringes. The 0.35 nm fringes spacing corresponding to the (101) plane of TiO_2(A), while lattice spacing of about 0.25 nm corresponds to the (101) plane of ZnO, which indicated the formation of TiO_2(A)/ZnO heterojunctions for sample TV-2.

X-ray photoelectron spectroscopy (XPS) is a surface-sensitive technique used to confirm the presence and chemical states of Ti, Zn, and O in the samples. Fig. 3 shows the survey and high-resolution XPS spectra of Zn 2*p*, Ti 2*p*, and O 1*s* of samples TV-4, TB-3, TV-3, and TV-2; fitting results of the experimental data for Ti 2*p* and O 1*s* for TV-4 are also shown.

Fig. 3a shows the XPS survey spectra of the samples, which indicated the presence of Ti, Zn, O, and C. The peak intensities of Ti and Zn differed among the samples obtained under different preparation processes and Ti/Zn molar ratios; such results reveal that the Ti and Zn contents change with variations in preparation process and Ti/Zn molar ratio. According to the peak intensities of Ti and Zn, the molar ratios of Ti/Zn were estimated and the results are 4, 3, 2 and 1 for sample TV-4, TB-3, TV-3 and TV-2, respectively. Fig. 3b shows the high-resolution spectrum of Zn 2*p*. Peaks at 1022.0 and 1045.1 eV were ascribed to Zn $2p_{3/2}$ and Zn $2p_{1/2}$, respectively. The peak separation between Zn $2p_{3/2}$ and Zn $2p_{1/2}$ was 23.1 eV, which was assigned to the +2 oxidation state of Zn [28]. The Ti 2*p* high-resolution XPS spectrum (Fig. 3c) shows two peaks at binding energies of approximately 458.1 (Ti $2p_{3/2}$) and 463.9 (Ti $2p_{1/2}$) eV. Pure TiO_2 exhibited typical binding energies at 459.4 and 464.7 eV corresponding to the binding energies of Ti $2p_{3/2}$ and Ti $2p_{1/2}$, respectively. The Ti 2*p* peak showed slight deformation at the lower side of the binding energy, which corresponds to the different oxidation states of Ti and strong electronic interactions between Zn and Ti atoms in the mixed oxide structure [29]. Fitting results of the Ti $2p_{3/2}$ peak revealed the presence of a major peak at 458.1 eV with a shoulder at 457.6 eV. The Ti $2p_{1/2}$ peak was deconvoluted into two binding energies at 463.9 and 463.2 eV. The peaks at 458.1 and 463.9 eV were assigned to the $2p_{3/2}$ and $2p_{1/2}$ core levels of Ti^{4+}, respectively. Peaks at 457.6 and 463.2 eV were ascribed to the $2p_{3/2}$ and $2p_{1/2}$ core levels of Ti^{3+}, respectively (Fig. 3d). The shifts were attributed to the existence of Ov around Ti^{4+}. Ti^{3+} species were formed in the heterojunction samples to satisfy the requirement of charge equilibrium. Shifts of the Ti 2*p* peak to lower energies differed with changes in preparation conditions, which indicate that different processes and Ti/Zn molar ratios influence the concentration of Ti^{3+}. Ti^{3+} is essentially a defective state and acts as a hole trap to enhance charge separation and suppress recombination of electron–hole pairs [30].

The high-resolution O 1*s* spectra of samples TV-4, TB-3, TV-3, and TV-2 are shown in Fig. 3e. The regions of XPS spectra include a main peak with a binding energy of 529.5 eV and a minor peak with a binding energy of 531.1 eV. Primary and secondary peaks were attributed to lattice oxygen in TiO_2, $ZnTiO_3$, and ZnO (i.e., Ti–O and Zn–O) and oxygen in surface hydroxyl groups (i.e., Ti–OH and Zn–OH), respectively [31]. Peak separation of the O 1*s* spectrum for TV-4 exhibited three types of oxygen bands with binding energies of 529.5, 531.1, and 532.2 eV (Fig. 3f). The band at 529.5 eV was attributed to Ti(IV)–O and Zn(II)–O bonds, and bands at 531.1 eV were attributed to Ti–OH and Zn–OH [32]. The peak observed at 532.2 eV corresponded to surface defects, such as Ov (surface Ti^{3+}). On the one hand, these defects can act as hole traps to enhance charge transfer and catalytic activity and suppress recombination of electron–hole pairs [30]. On the other hand, abundant adsorbed water and hydroxyl groups on the surface can potentially trap holes to form important oxidative •OH for photodegradation of organic molecules [33].

3.2. Formation of Ti^{3+} self-doped titanium–zinc hybrid oxides

XRD and TEM results indicate that the compositions and morphologies of the samples change dramatically with changes in Ti/Zn molar ratio and preparation process. XPS results show that the content and chemical state of Ti and Zn differ among the samples

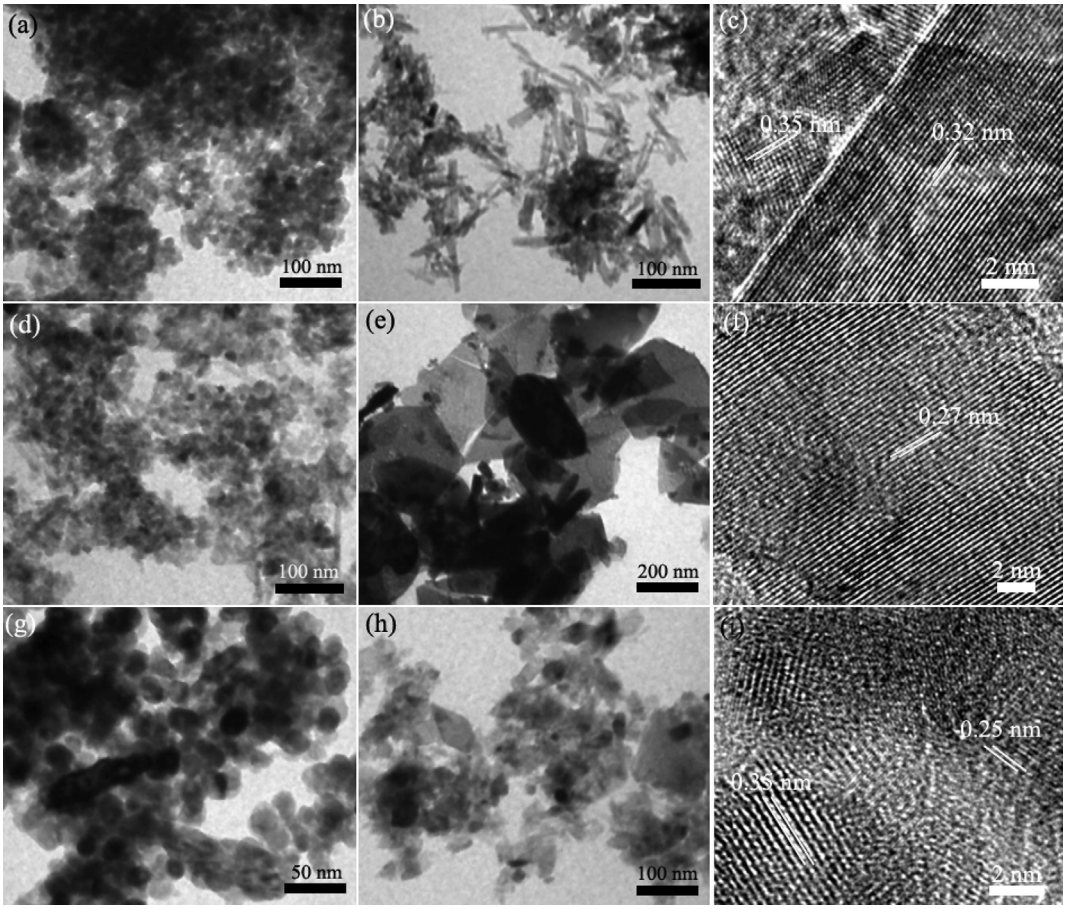

Fig. 2. TEM and HRTEM images of the samples obtained at different process and Ti/Zn molar ratio.

obtained under different conditions. When the molar ratio of Ti/Zn was 4:1, no ZnO or $ZnTiO_3$ were detected in the samples and the obtained TiO_2 showed a unique crystalline structure. As the molar ratio of Ti/Zn decreased, $ZnTiO_3$ and ZnO began to appear in the sample. However, the proportions of TiO_2 to $ZnTiO_3$ and ZnO differed among samples obtained from different synthesis procedures. This finding indicates that different processes and Ti/Zn molar ratios influence the phase composition and morphology of the resultant samples. As such, we analyzed the formation process of the samples.

Based on the conventional electrode potentials (TiO^{2+}/Ti^{3+}, $\varphi^{\theta}_{A} = 0.1$ V, Ti^{3+}/Ti^{2+}, $\varphi^{\theta}_{A} = -0.37$ V, Zn^{2+}/Zn, $\varphi^{\theta}_{A} = -0.76$ V), Ti^{4+} is easily reduced to Ti^{3+} and even to Ti^{2+} by Zn. Given that $Ti(SO_4)_2$ is a strong acid–weak base salt, its aqueous solution is acidic. When Zn powder is added to the $Ti(SO_4)_2$ solution, the following reactions mainly occur:

$$2Ti^{4+} + Zn = 2Ti^{3+} + Zn^{2+} \quad (1)$$

$$Zn + 2H^{+} = Zn^{2+} + H_2 \quad (2)$$

As the reaction progressed, the concentrations of Ti^{3+} and Zn^{2+} and the pH increased at the same time. Given that the K_{sp} of $Ti(OH)_3$ (1.0×10^{-40}) and $TiO(OH)_2$ (1×10^{-29}) is far lower than that of $Zn(OH)_2$ (2.09×10^{-16}), the initial precipitation pH values of Ti^{4+} and Ti^{3+} are lower than that of Zn^{2+}. Therefore, when the molar ratio of Ti/Zn was 4, the first black precipitate generated was $Ti(OH)_3$ and $TiO(OH)_2$. The sample obtained from the black precipitate was Ti^{3+} self-doped anatase TiO_2 (Fig. 1; TB-4). When NaOH solution was added to the filtrate and the pH was adjusted to 5,6, the concentrations of Ti^{3+}, Ti^{4+}, and Zn^{2+} in the filtrate precipitation increased at the same time. However, given that the concentration of Zn^{2+} in the solution was low, $Zn(OH)_2$ existed among $Ti(OH)_3$ and $TiO(OH)_2$ as a crystal nucleus. During heat treatment, the ZnO crystal nucleus generated accelerates the phase transformation of anatase TiO_2 to rutile TiO_2. As such, the sample obtained was a TiO_2(A)/TiO_2(R) heterojunction (Fig. 1; TV-4). The XRD patterns of the samples (Fig. 1; TB-4 and TV-4) failed to exhibit Zn oxides and Ti^{4+} is hardly replaced by Zn^{2+} because of the large difference in their ionic radii (Zn^{2+}, 0.88 Å; Ti^{4+}, 0.745 Å). Therefore, Zn could primarily exist in the form of ZnO clusters or as an amorphous material on the TiO_2 surface [34]. Zn^{2+} may weaken surface oxygen bonds, thereby increasing the probability of oxygen loss from the surface. The remaining electrons may be trapped at Ti^{4+} interstitial sites to form Ti^{3+} [35]. Mair et al. reported that increases in Ov concentration can enhance nucleation process and that metal doping can enhance anatase-to-rutile transformation by increasing Ov concentrations [36]. Thus, the tunable two-phase structure may be attributed to the synergistic effects of Zn doping and oxygen vacancies [37]. Zn^{2+} can affect the structure of O–Ti–O bonds and favor TiO_2(R) nanorod formation from amorphous titania and TiO_2(A) [38].

When the molar ratio of Ti/Zn reached 3:1, the black precipitate was mainly composed of $Ti(OH)_3$ and $TiO(OH)_2$. When the concentration of Zn^{2+} increased, the concentration of $Zn(OH)_2$ in the precipitate also increased. Moreover, a small amount of $ZnTiO_3$ was generated during subsequent heat treatment. At this time, the morphology of TiO_2 consisted of irregularly aggregated

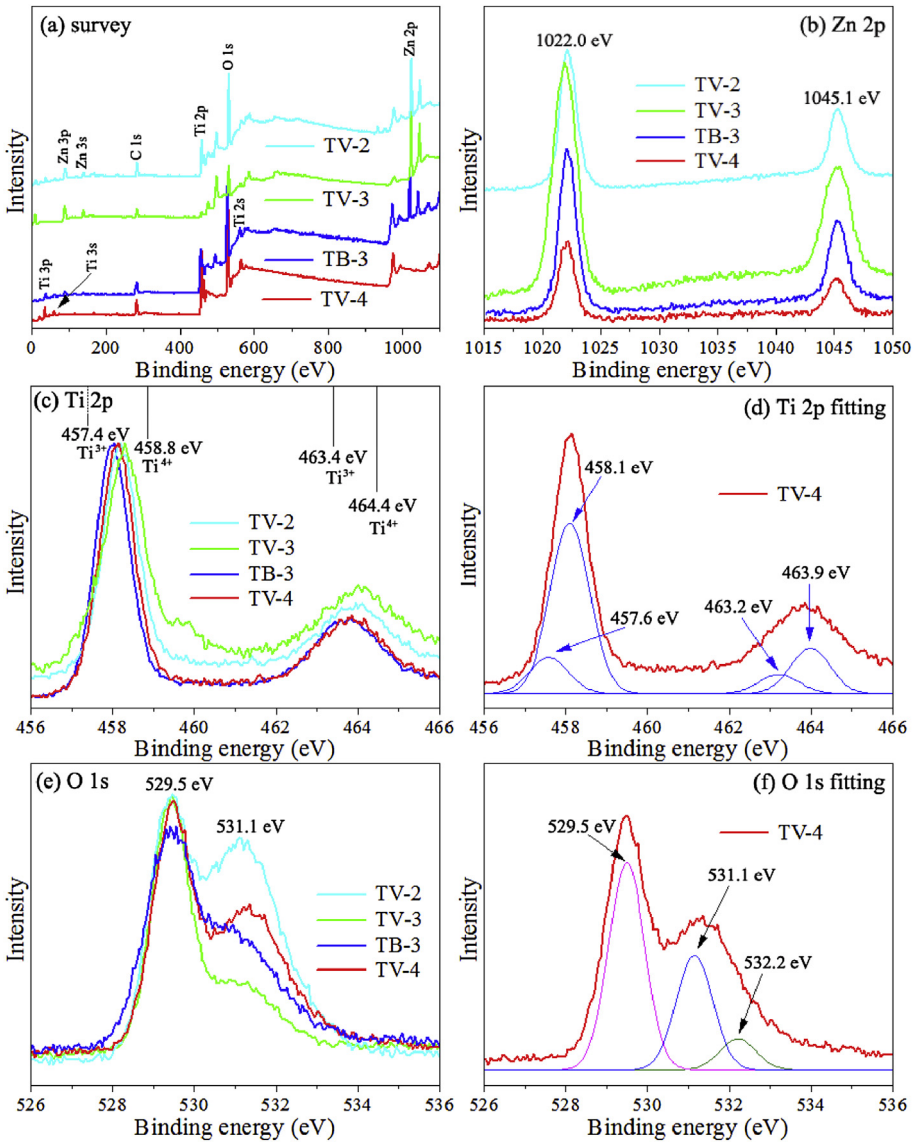

Fig. 3. XPS spectra of TV-4, TB-3, TV-3 and TV-2: (a) survey spectrum and high resolution XPS spectra for (b) Zn 2p, (c) Ti 2p, and (e) O 1s; fitting results of the experimental data for (d) Ti 2p and (f) O 1s for sample TV-4.

nanoparticles while $ZnTiO_3$ consisted of irregular nanoflakes. A large amount of Zn^{2+} remained in the filtrate. When NaOH was added to adjust the solution pH, the remaining Ti^{3+}, Ti^{4+}, and Zn^{2+} in the solution precipitated concurrently. Thus, $ZnTiO_3$ was the primary product obtained after heat treatment. The flake-like morphology of this produce became prominent, which indicates that intergrowth of $ZnTiO_3$ nanoflakes occurs as the Zn^{2+} concentration increases in the system. When $Ti(OH)_3$, $TiO(OH)_2$, and $Zn(OH)_2$ were completely mixed, hexagonal-phase $ZnTiO_3$ was obtained under low heat treatment. When the molar ratio of Ti/Zn reached 2:1, Zn powder did not entirely react with Ti^{4+} under low-acidity conditions. As such, the black precipitate contained metal Zn (Fig. 1; TB-2). When NaOH solution was added to the filtrate, a large amount of $Zn(OH)_2$ and small amounts of $Ti(OH)_3$ and $TiO(OH)_2$ were observed in the bluish violet precipitate. Given that the proportions of $Ti(OH)_2$, $TiO(OH)_2$, and $Zn(OH)_2$ were not balanced, $ZnTiO_3$ cannot be obtained. However, corresponding oxides were generated, and the obtained product was composed of both ZnO and TiO_2 (Fig. 1; TV-2).

3.3. Optical properties and photocatalytic activity

Fig. 4 shows the UV–Vis diffuse reflectance spectra of pure $ZnTiO_3$, TiO_2, and samples obtained via different precipitation processes and with Ti/Zn molar ratios. The spectra of the experimental samples show a redshift compared with those of pure $ZnTiO_3$, TiO_2 and exhibit broad absorption bands between 400 and 800 nm covering the entire visible-light range. This redshift and enhanced visible-light absorption may be attributed to Ti^{3+} self-doping effects as well as synergistic interactions between TiO_2, $ZnTiO_3$, and ZnO in the heterojunction samples. Ti^{3+} species can introduce localized states in the forbidden band gap of TiO_2 at approximately 0.75–1.18 eV below the conduction band (CB) edge of TiO_2 such that absorption expands to the visible-light region [39]. Thus, for the present Ti^{3+} self-doped titanium–zinc hybrid oxides, the minimum energy required for excitation of an electron from the valence band (VB) to the CB is considerably higher than those required for pure TiO_2, $ZnTiO_3$, and ZnO. The degree of red-shifting and absorption intensity in the visible-light range

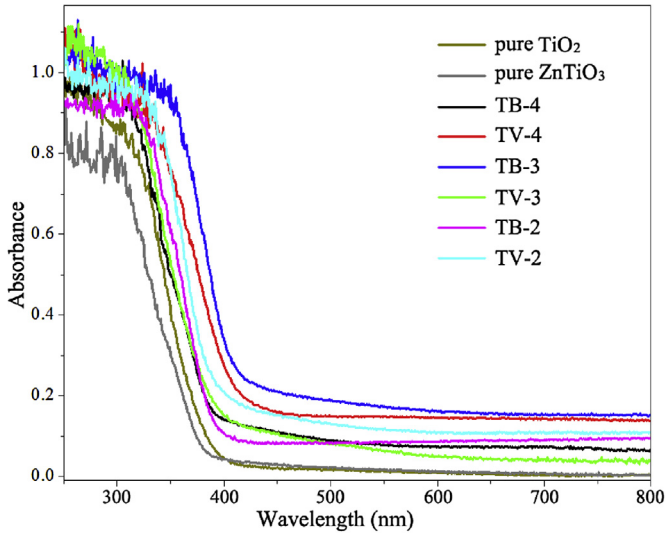

Fig. 4. UV–Vis DRS spectra of pure $ZnTiO_3$, TiO_2 and the samples obtained at different precipitation process and Ti/Zn molar ratio.

differed among the samples obtained under different conditions, which indicates that the Ti^{3+} content and proportion of titanium–zinc oxide are different in the samples. Although TB-2 showed strong absorption in the visible-light region, its absorption in the UV region was weaker than those of other samples. We believe that the strong absorbance of TB-2 in the visible-light region may be attributed to unreacted Zn powder in the sample. As shown in Fig. 1, the characteristic diffraction peaks of Zn may be detected in sample TB-2. Regardless of these slight variations in absorption, enhanced light adsorption of the Ti^{3+} self-doped titanium–zinc hybrid oxides allows full utilization of visible light and results in production of more electron–hole pairs under visible-light illumination and, ultimately, higher photocatalytic activity.

As a common xanthene dye, RhB is often used as a test model pollutant in semiconductor photocatalysis. Fig. 5a shows the adsorption and photodegradation abilities of the prepared Ti^{3+} self-doped titanium–zinc hybrid oxide samples on RhB solutions in comparison with those of pure TiO_2 and $ZnTiO_3$. The Ti^{3+} self-doped titanium–zinc hybrid oxide samples exhibited excellent adsorption and visible-light photocatalytic activities compared with those of pure TiO_2 and $ZnTiO_3$. Prior to switching the light on, the concentrations of RhB in the presence of the experimental samples were depleted faster than those in pure TiO_2 and $ZnTiO_3$. In particular, TB-4 exhibited specific adsorption capacity because its crystalline structure is relatively weak and its particle size is fairly small (Figs. 1 and 2). Thus, sample TB-4 should have the largest surface area among the samples obtained.

After switching the light on, all samples showed higher photocatalytic activity under visible light compared with pure TiO_2 and $ZnTiO_3$. This finding may be attributed to the properties of Ti^{3+} self-doped TiO_2 and $ZnTiO_3$ or ZnO composites. Among the samples obtained, TB-3 showed the highest visible-light photocatalytic activity.

The photocatalytic activity of the powders can be quantitatively evaluated by comparing their apparent reaction rate constants. The photocatalytic oxidation of organic pollutants in aqueous suspensions follows the Langmuir–Hinshelwood model [40], which is expressed as follows:

$$\ln\left(\frac{C_0}{C_t}\right) = k_{app} \times t$$

where C_t is the concentration of aqueous RhB at reaction time t, C_0 is the initial concentration of RhB, and k_{app} is the first-order rate constant. The first-order rate constant k_{app} could be obtained from the linear time dependences of $\ln(C/C_0)$, as shown in Fig. 5b. The k_{app} values for pure TiO_2, $ZnTiO_3$, TB-4, TV-4, TB-3, TV-3, TB-2, and TV-2 calculated based on the data in Fig. 5b were 0.0029, 0.0028, 0.015, 0.0271, 0.0325, 0.0105, 0.0101, and 0.0213 min^{-1}, respectively. We note that: (1) under visible-light irradiation, the rate constants of RhB degradation followed the sequence: TB-3 > TV-4 > TV-2 > TB-4 > TV-3 > TB-2 > pure TiO_2 > pure $ZnTiO_3$ and (2) TB-3 showed a first-order rate constant of $k_{app} = 0.0325$, which is approximately 11.2 and 11.6 times greater than those of pure TiO_2 and $ZnTiO_3$, respectively, under visible-light irradiation.

Detection of the main oxidative species in a photocatalytic process is important for elucidating the photocatalytic mechanism. The main oxidative species in the photocatalytic process can be detected by trapping radicals and holes in experiments involving the use of 1.0 mM *tert*-butanol (TBA, a quencher of •OH), ammonium oxalate (AO, a quencher of h^+), and *p*-benzoquinone (BQ, a quencher of $\bullet O_2^-$) [41]. As shown in Fig. 6a, addition of AO induced only a small change in RhB photodegradation in the TB-3 system. When the •OH scavenger (TBA) was added to the experimental systems, photocatalytic performance evidently decreased. The photocatalytic activity of the TB-3 sample was significantly suppressed by addition of the $\bullet O_2^-$ scavenger (BQ). Thus, $\bullet O_2^-$ radicals are mainly responsible for RhB photodegradation, followed by •OH and finally h^+.

•OH radicals can react with terephthalic acid (TA) in basic solution to generate 2-hydroxyterephthalic acid, which emits a unique fluorescence signal with an emission peak at approximately 426 nm [42]. The fluorescence intensity is directly proportional to the amount of •OH radicals formed in water. The larger the formation of •OH radicals, the higher the separation rate of electron–hole pairs in the photocatalysts [43]. Fig. 6b shows the photoluminescence (PL) emission spectra obtained upon excitation of the TA solution at 320 nm; here, spectra were obtained after every 10 min of illumination. The PL intensity and number of •OH at approximately 426 nm gradually increased with the irradiation time. The maximum number of •OH radicals was formed by using the TB-3 samples during photoreaction; this finding agrees the results of RhB photodegradation (Fig. 5a). Linear correlations between fluorescence intensity and irradiation time (inset in Fig. 6b) confirm the good stability of Ti^{3+} self-doped titanium–zinc hybrid oxides. These results clearly indicate that Ti^{3+} self-doped titanium–zinc hybrid oxides exhibit considerably higher photocatalytic activities than P25 TiO_2 and $ZnTiO_3$; such high activity can be attributed to improvements in photogenerated electron–hole separation and extension of the lifetimes of photogenerated carriers [8].

3.4. Photoelectrochemical and hydrogen evolution properties

Photocurrent measurements provide a direct value to determine the separation efficiency of the photoinduced electrons and holes and estimate the electronic interaction in the resultant photoanodes. The higher the photocurrent was, the better the electron and hole separation efficiency would be [44]. Linear sweeps voltammetric technique and transient photocurrent density responses against the time were used to study the photocurrent properties of the different photoanodes electrode in 0.25 M Na_2S and 0.35 M Na_2SO_3 aqueous solution with visible-light illumination at a scanning rate of 0.02 V s^{-1} and a fixed potential bias of +1.0 V versus saturated calomel electrode (SCE). For comparison, the photoelectrochemical responses of pure TiO_2 and $ZnTiO_3$ were also determined. Fig. 7(a) shows that, under visible-light illumination,

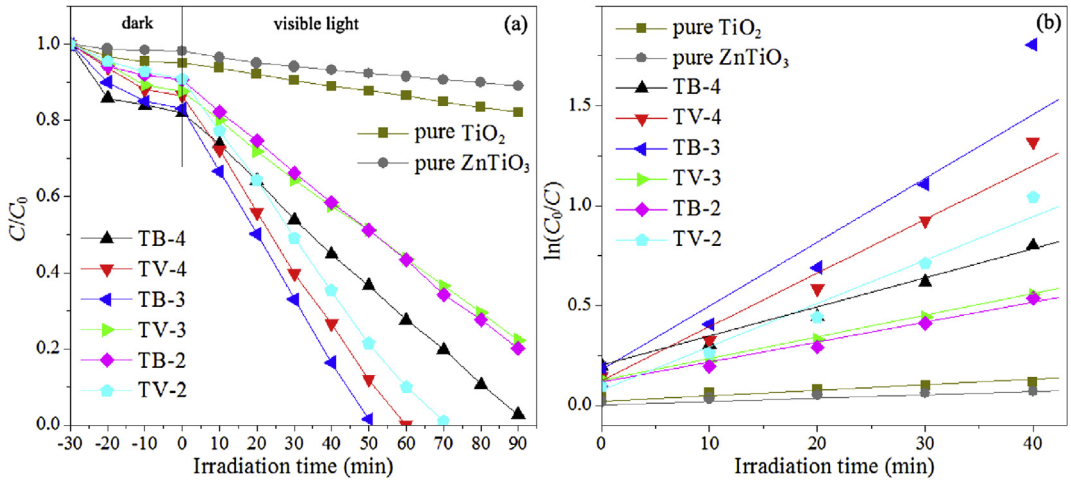

Fig. 5. (a) The photodegradation of RhB solutions by using pure TiO_2, $ZnTiO_3$ and Ti^{3+} self-doped titanium–zinc hybrid oxides as photocatalyst under visible light irradiation in neutral suspension. (b) Variation in the normalized $\ln(C/C_0)$ of the RhB concentration as a function of visible-light irradiation time.

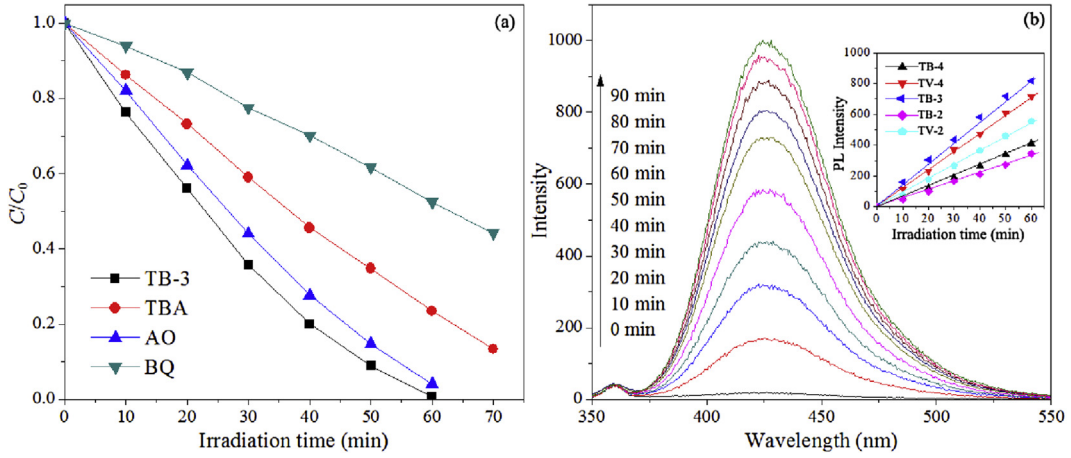

Fig. 6. (a) Photodegradation efficiency of RhB on sample TB-3 by added the active species capture. (b) •OH trapping in the PL spectra during irradiation by using sample TB-3 in a 5×10^{-4} M TA solution (excitation wavelength, 320 nm). Inset: Temporal dependence of the fluorescence intensity at 426 nm of visible-light irradiated using the TB-4, TV-4, TB-3, TB-2 and TV-2 samples.

the pure TiO_2 and $ZnTiO_3$ photoanodes yielded relatively low photocurrent densities. On the contrary, the Ti^{3+} self-doped titanium–zinc hybrid oxides photoanodes showed increased photocurrent density.

The transient photocurrent response of different photoelectrodes were measured under a visible light pulse of 50s. Fig. 7(b) compares the transient photocurrent response of different samples. The pure TiO_2 and $ZnTiO_3$ photoanodes only generates a negligible photocurrent under the visible light illumination, which can be easily explained by their poor optical light absorption properties. The Ti^{3+} self-doped titanium–zinc hybrid oxides photoanodes exhibit significant enhancements in photocurrent, which may be attributed to the formation of the TiO_2(A)/TiO_2(R), TiO_2(A)/TiO(R)/$ZnTiO_3$, TiO_2(A)/ZnO heterojunction structure and exists of Ti^{3+}. When the light was turned off, the current rapidly decayed to a lower level, indicating that the current was completely due to the activity of the photoanode and that charge transport was very fast. These results indicated that the Ti^{3+} self-doped titanium–zinc hybrid oxides signifies an improved optical absorption capability, enhanced separation of photoinduced electrons and holes and suppressed the recombination of electron and holes.

The photocurrents of the TV-4 and TB-3 photoanodes were significantly enhanced compared with those of the other photoanodes, indicating that the separation and transport efficiencies of photogenerated electron–hole pairs were much higher than those other photoanodes. This is mainly attributed to the TiO_2(A)/TiO_2(R), TiO_2(A)/TiO_2(R)/$ZnTiO_3$ heterojunction structure and exists of Ti^{3+}. The heterojunction structure can promote the separation of photoinduced electrons and holes, the Ti^{3+} can improve the electron conductivity and absorb visible light [20]. Therefore, the heterojunction has a high transport rate and a lower recombination of photoinduced electrons and holes.

The Ti^{3+} self-doped titanium–zinc hybrid oxides photoanodes show advanced enhanced light absorption and fast charge separation with a low recombination rate, which indicate a promisingly photoanode for water splitting. Fig. 8 shows the hydrogen evolution abilities of the prepared Ti^{3+} self-doped titanium–zinc hybrid oxide photoanodes in comparison with pure TiO_2 held at 0.4 V vs. saturated calomel electrode. The Ti^{3+} self-doped titanium–zinc hybrid oxide samples exhibited excellent hydrogen evolution activity compared with those of pure TiO_2. Sample TB-3 presents the most excellent activity at 0.4 V vs. saturated calomel electrode, producing about 68 μmol h^{-1} H_2 with an almost constant rate during 9 h.

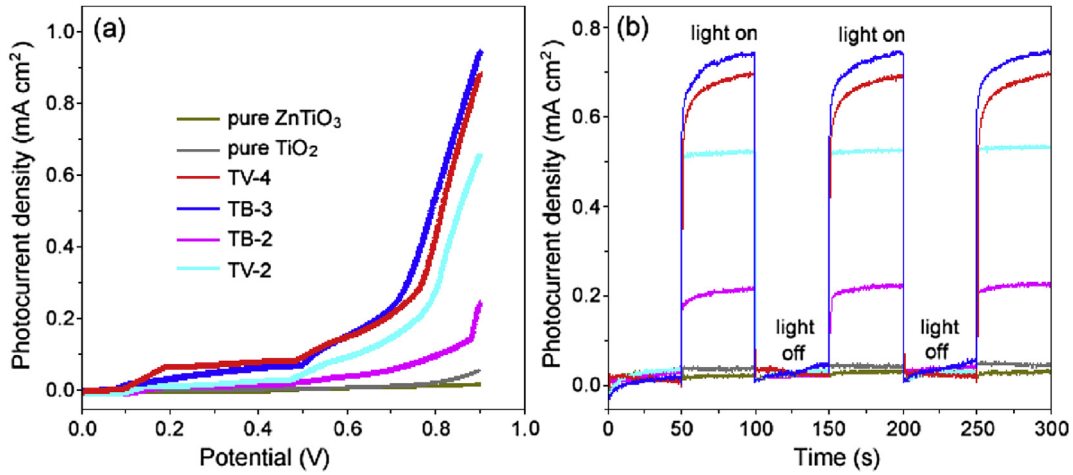

Fig. 7. (a) Linear sweeps voltammograms and (b) Comparison of transient photocurrent response of the different photoanodes under visible light irradiation with 0.25 M Na_2S and 0.35 M Na_2SO_3 aqueous solution as electrolyte at 0.4 V vs. SCE.

3.5. Proposed mechanism for the enhanced photoelectrochemical and photocatalytic performance

The aforementioned results demonstrate that our samples are Ti^{3+} self-doped titanium–zinc hybrid oxides. Along with changes in preparation conditions, the structure, morphology, and composition of the samples also changed, leading to different optical properties, photoelectrochemical and visible-light photocatalytic performances. When the molar ratio of Ti/Zn was 4:1, the samples were mainly composed of TiO_2(A) or TiO_2(A)/TiO_2(R) and contain trace amounts of Zn^{2+}. When the molar ratio of Ti/Zn was 3:1, the sample was composed of TiO_2(A), TiO_2(R), and ZnTiO3. When the molar ratio of Ti/Zn reached 2:1, the sample was composed of TiO_2(A) and ZnO. Photoelectrochemical and photocatalytic activity mainly depends on effective separation of electron–hole pairs. Appropriate proportions of Ti^{3+} self-doped anatase and/or rutile TiO_2 and $ZnTiO_3$ or ZnO can form suitable heterojunctions, such as TiO_2(A)/TiO_2(R), TiO_2(A)/TiO_2(R)/$ZnTiO_3$, or TiO_2(A)/ZnO, and speed up separation of electrons and holes. In addition, Ti^{3+} and Ov perform essential functions in photocatalytic processing over TiO_2-based photocatalysts. Ti^{3+} doping extends the absorption of TiO_2 to the visible-light region, and Ov on the particle surface can adsorb oxygen molecules and be used as an electron capture agent, thereby reducing the electron–hole pair recombination rate [45,46].

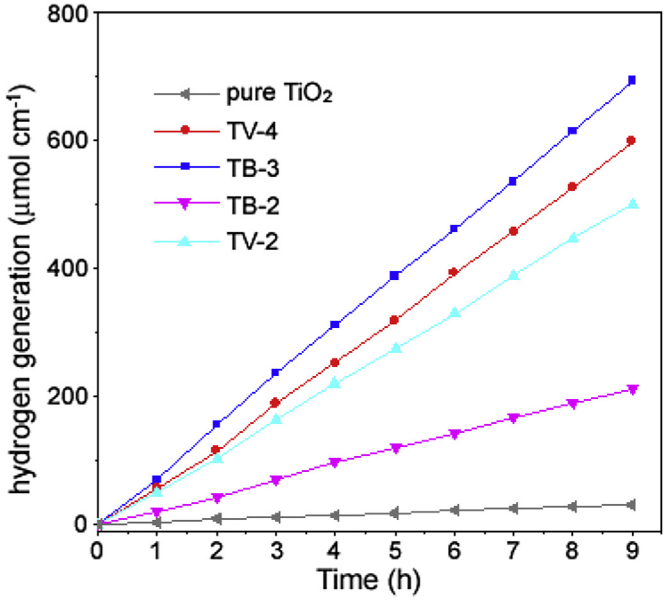

Fig. 8. The hydrogen evolution activities of the different electrode under visible-light illumination measured at 0.4 V vs. saturated calomel electrode.

In addition, photodegradation results (Fig. 5a) indicate that pure TiO_2 and $ZnTiO_3$ exhibit slight visible-light photocatalytic activity. Pure TiO_2 and $ZnTiO_3$ semiconductors have a wide band gap that cannot be directly excited by visible-light illumination. Therefore, visible-light photocatalytic activity may be attributed to dye sensitization of RhB. Electrons in the highest occupied molecular orbital of RhB molecules could be excited to the lowest unoccupied molecular orbital under visible-light irradiation to generate the excited-state RhB* [47]. RhB* donates electrons to the CB of TiO_2 or $ZnTiO_3$, where electrons are scavenged by molecular oxygen to yield $\cdot O_2^-$ radical anions and oxidize RhB molecules [48]. The enhanced photoelectrochemical and photocatalytic activities of Ti^{3+} self-doped titanium–zinc hybrid oxides compared with those of pure TiO_2 and $ZnTiO_2$ are attributed to the following reasons: (i) Ti^{3+} self-doping extends the absorption of TiO_2 to the visible-light region and accelerates the electron transfer rate; (ii) appropriate proportions of Ti^{3+} self-doped anatase and rutile TiO_2, $ZnTiO_3$, or ZnO in the titanium–zinc hybrid oxide composites form suitable heterojunctions and speed up separation of electron–hole pairs at the heterojunction interface; and (iii) photocatalytic activity is enhanced by hydroxyl groups on the particle surface. A possible mechanism of the charge separation process of the Ti^{3+} self-doped titanium–zinc hybrid oxides is shown in Fig. 9.

Fig. 9 shows that the presence of Ti^{3+} and Ov introduces continuous states between the VB and CB of TiO_2(A + R) that extend the absorption of TiO_2 to the visible-light region (Fig. 4). Under visible-light irradiation, the electrons could be excited from the VB of TiO_2 to the continuous states, progressively shifting to the CB of TiO_2 [Fig. 9(1)]. When the molar ratio of Ti/Zn was 4:1, the sample obtained from the black precipitate was anatase TiO_2 (Fig. 1; TB-4), and separation of photoinduced electrons and holes is shown in Fig. 9a. The sample obtained from the bluish violet precipitate was anatase and rutile TiO_2 (Fig. 1; TV-4), and separation of photoinduced electrons and holes is shown in Fig. 9b [26]. Differences between the band edges of the two TiO_2 phases could appropriately facilitate charge transfer [49]. Photoexcited electrons in TiO_2(R) migrate to the CB of TiO_2(A), whereas holes in TiO_2(A) migrate to the VB of TiO_2(R) [Fig. 9(4)]. These results imply that electron–hole recombination is suppressed. When the molar ratio of Ti/Zn was

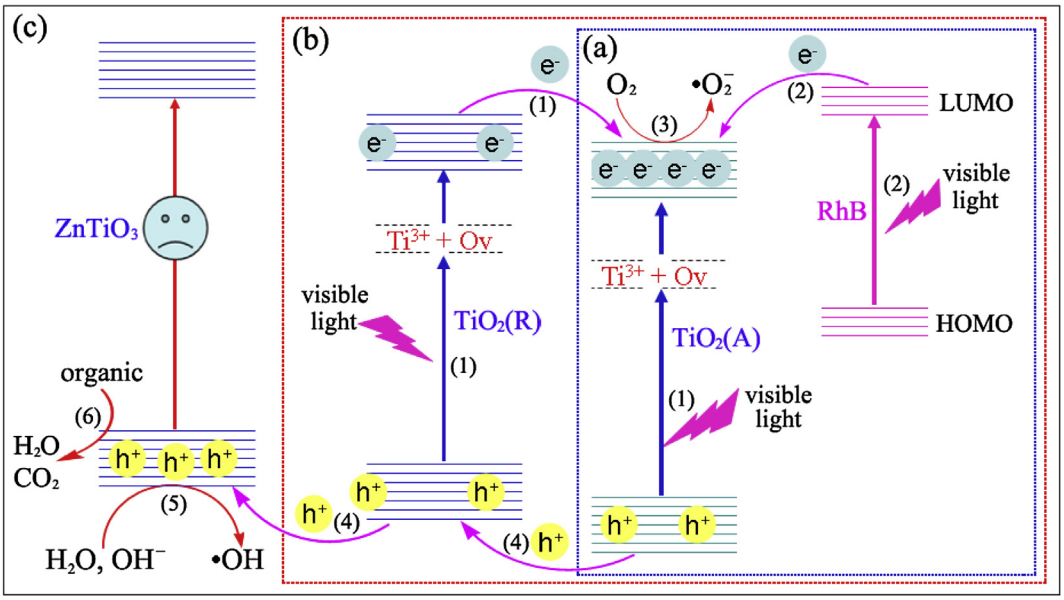

Fig. 9. Synergetic mechanism of the visible-light response and separation of electron–hole pairs of Ti^{3+} self-doped titanium–zinc hybrid oxides systems.

3:1, the samples were composed of anatase, rutile phase TiO_2, and $ZnTiO_3$ (Fig. 1; TB-3 and TV-3), and separation of photoinduced electrons and holes is shown in Fig. 9c. Electrons were transferred from the CB of rutile TiO_2 to the CB of anatase TiO_2, and holes were transferred from the VB of anatase TiO_2 to the VB of rutile TiO_2 and then to the VB of $ZnTiO_3$ [Fig. 9(4)], thereby inhibiting recombination of electron–hole pairs and increasing their lifetimes [50].

When the molar ratio of Ti/Zn was 2:1, the samples were composed of anatase TiO_2 and ZnO (Fig. 1; TB-2 and TV-2). Under visible-light irradiation, electrons are excited from the VB of anatase TiO_2 to continuous states, progressively shifting to the CB of TiO_2(A). Holes are transferred from the VB of anatase TiO_2 to the VB of ZnO [51]. In all cases, adsorbed RhB molecules were excited to form the excited-state RhB* and subsequently injected electrons to the CB of anatase TiO_2 [Fig. 9(2)]. The excited-state electrons transferred to the TiO_2 surface to react with dissolved oxygen, generate the main active groups of superoxide anion radicals ($\bullet O_2^-$), and further oxidize RhB [Fig. 9(3)]. In addition, holes at the VB of $ZnTiO_3$ can simultaneously oxidize the surface OH^- and H_2O groups to generate •OH [Fig. 9(5)] and/or directly oxidize organic molecules [Fig. 9(6)]. These highly active species (e.g., $\bullet O_2^-$, •OH, and h^+) mainly cause RhB degradation [52]. The relevant reactions may be expressed as follows:

$$TiO_2(A)/TiO_2(R) + h\upsilon \rightarrow TiO_2\,(e^-) + TiO_2\,(h^+) \quad (3)$$

$$RhB/TiO_2 + h\upsilon \rightarrow TiO_2\,(e^-) + RhB^* \quad (4)$$

$$O_2 + e_{CB}^- \rightarrow \bullet O_2^- \quad (5)$$

$$TiO_2(h^+)/ZnTiO_3 \rightarrow TiO_2 + ZnTiO_3\,(h^+) \quad (6)$$

$$H_2O/OH^- + h^+ \rightarrow \bullet OH + h^+ \quad (7)$$

4. Conclusions

In summary, Ti^{3+} self-doped titanium–zinc hybrid oxides with different phase compositions and morphologies were successfully synthesized using Zn as the reductant and Zn source by a chemical–reduction precipitation method and subsequent thermal treatment. Ti^{3+} self-doping enhanced the photoabsorption capability and photoelectrochemical performance of titanium–zinc hybrid oxides in the visible-light region. Moreover, the Ti/Zn molar ratio influenced the structure, morphology, and composition of the final products. Heterojunctions formed at the interfaces of TiO_2(A)/TiO_2(R), $ZnTiO_3$/TiO_2(A) and TiO_2/ZnO exhibited redshifted absorption and improved separation efficiency of charge carriers, thereby improving the water splitting and photocatalytic activities of the final products compared with those of pure TiO_2 and $ZnTiO_3$ under visible-light irradiation. Our experimental results provide meaningful guidance for future developments of potential Ti-based photocatalytic composite materials for water splitting and organic pollutant degradation under solar irradiation.

Acknowledgments

This work was supported by the Key Project of Natural Science Foundation of Shandong Province (ZR2013EMZ001), the National Basic Research Program of China (Grant No. 2013CB632401), the National Nature Science Foundation of China (51402145) and the Project of Shandong Province Higher Educational Science and Technology Program (J12LA01). This research has been partially supported by the Program for Scientific Research Innovation Team in Colleges and Universities of Shandong Province. This work was also supported by the U.S. Department of Energy under Contract DE-AC0206CH11357 with the main support provided by the Vehicle Technologies Office, Department of Energy (DOE) Office of Energy Efficiency and Renewable Energy (EERE).

References

[1] A. Kubacka, M. Fernández-García, G. Colón, Advanced nanoarchitectures for solar photocatalytic applications, Chem. Rev. 112 (2012) 1555–1614.
[2] X.L. Zhang, Y. Li, J.L. Zhao, S.G. Wang, Y.D. Li, H.T. Dai, X.W. Sun, Advanced three-component ZnO/Ag/CdS nanocomposites photoanode for photocatalytic water splitting, J. Power Sources 269 (2014) 466–472.
[3] Q.Y. Wang, J.L. Qiao, R.C. Jin, X.H. Xu, S.M. Gao, Fabrication of plasmonic AgBr/Ag nanoparticles-sensitized TiO_2 nanotube arrays and their enhanced photoconversion and photocatalytic properties, J. Power Sources 277 (2015) 480–485.

[4] H.F. Lin, L.P. Li, M.L. Zhao, X.S. Huang, X.M. Chen, G.S. Li, R.C. Yu, Synthesis of high-quality brookite TiO_2 single-crystalline nanosheets with specific facets exposed: tuning catalysts from inert to highly reactive, J. Am. Chem. Soc. 134 (2012) 8328–8331.

[5] Y.F. Huang, Y.L. Wei, J.H. Wu, C.S. Guo, M. Wang, S. Yin, T. Sato, Low temperature synthesis and photocatalytic properties of highly oriented ZnO/$TiO_{2-x}N_y$ coupled photocatalysts, Appl. Catal. B Environ. 123–124 (2012) 9–17.

[6] S.T. Nishanthi, S. Iyyapushpam, B. Sundarakannan, E. Subramanian, D.P. Padiyan, Plasmonic silver nanoparticles loaded titania nanotubes arrays exhibiting enhanced photoelectrochemical and photocatalytic activities, J. Power Sources 274 (2015) 885–893.

[7] K. Pan, Y.Z. Dong, W. Zhou, Q.J. Pan, Y. Xie, T.F. Xie, G.H. Tian, G.F. Wang, Facile fabrication of hierarchical TiO_2 nanobelt/ZnO nanorod heterogeneous nanostructure: an efficient photoanode for water splitting, ACS Appl. Mater. Interfaces 5 (2013) 8314–8320.

[8] L. Wu, J. Xing, Y. Hou, F.Y. Xiao, Z. Li, H.G. Yang, Fabrication of regular ZnO/TiO_2 heterojunctions with enhanced photocatalytic properties, Chem. Eur. J. 19 (2013) 8393–8396.

[9] R. Murugan, V.J. Babu, M.M. Khin, A.S. Nair, S. Ramakrishna, Synthesis and photocatalytic applications of flower shaped electrospun ZnO–TiO_2 mesostructures, Mater. Lett. 97 (2013) 47–51.

[10] S.Y. Guo, S. Han, H.F. Mao, S.M. Dong, C.C. Wu, L.C. Jia, B. Chi, J. Pu, J. Li, Structurally controlled ZnO/TiO_2 heterostructures as efficient photocatalysts for hydrogen generation from water without noble metals: the role of microporous amorphous/crystalline composite structure, J. Power Sources 245 (2014) 979–985.

[11] F.X. Xiao, Construction of highly ordered ZnO–TiO_2 nanotube arrays (ZnO/TNTs) heterostructure for photocatalytic application, ACS Appl. Mater. Interfaces 4 (2012) 7055–7063.

[12] D. Chen, H. Zhang, S. Hu, J. Li, Preparation and enhanced photoelectrochemical performance of coupled bicomponent ZnO–TiO_2 nanocomposites, J. Phys. Chem. C 112 (2008) 117–122.

[13] C.K. Xu, D. Gao, Two-stage hydrothermal growth of long ZnO nanowires for efficient TiO_2 nanotube-based dye-sensitized solar cells, J. Phys. Chem. C 116 (2012) 7236–7241.

[14] Y.S. Chang, Y.H. Chang, I.G. Chen, G.J. Chen, Y.L. Chai, Synthesis and characterization of zinc titanate nano-crystal powders by sol–gel technique, J. Cryst. Growth 243 (2012) 319–326.

[15] J.Z. Kong, A.D. Li, H.F. Zhai, H. Li, Q.Y. Yan, J. Ma, D. Wu, Preparation, characterization and photocatalytic properties of $ZnTiO_3$ powders, J. Hazard. Mater. 171 (2009) 918–923.

[16] S.J. Ke, X.S. Cheng, Q.H. Wang, Y.M. Wang, Z.D. Pan, Preparation of a photocatalytic TiO_2/$ZnTiO_3$ coating on glazed ceramic tiles, Ceram. Int. 40 (2014) 8891–8895.

[17] T. Surendar, S. Kumar, V. Shanker, Influence of La-doping on phase transformation and photocatalytic properties of $ZnTiO_3$ nanoparticles synthesized via modified sol–gel method, Phys. Chem. Chem. Phys. 16 (2014) 728–735.

[18] Y.Y. Cai, Y.X. Ye, Z.F. Tian, J. Liu, Y.S. Liu, C.H. Liang, In situ growth of lamellar $ZnTiO_3$ nanosheets on TiO_2 tubular array with enhanced photocatalytic activity, Phys. Chem. Chem. Phys. 15 (2013) 20203–20209.

[19] J.P. Wang, Z.Y. Wang, B.B. Huang, Y.D. Ma, Y.Y. Liu, X.Y. Qin, X.Y. Zhang, Y. Dai, Oxygen vacancy induced band-gap narrowing and enhanced visible light photocatalytic activity of ZnO, ACS Appl. Mater. Interfaces 4 (2012) 4024–4030.

[20] X. Liu, H. Xu, R.G. Lauren, S.M. Gao, Z.Z. Lou, W.J. Wang, B.B. Huang, Y. Dai, T. Xu, Ti^{3+} self-doped TiO_{2-x} anatase nanoparticles via oxidation of TiH_2 in H_2O_2, Catal. Today 225 (2014) 80–89.

[21] J.C. Wang, P. Liu, X.Z. Fu, Z. Li, W. Han, X.X. Wang, Relationship between oxygen defects and the photocatalytic property of ZnO nanocrystals in Nafion membranes, Langmuir 25 (2009) 1218–1223.

[22] M.Y. Guo, A.M.C. Ng, F.Z. Liu, A.B. Djurisic, W.K. Chan, H.M. Su, K.S. Wong, Effect of native defects on photocatalytic properties of ZnO, J. Phys. Chem. C 115 (2011) 11095–11101.

[23] A.B. Patil, K.R. Patil, S.K. Pardeshi, Enhancement of oxygen vacancies and solar photocatalytic activity of zinc oxide by incorporation of nonmetal, J. Solid State Chem. 184 (2011) 3273–3279.

[24] F. Zuo, L. Wang, T. Wu, Z.Y. Zhang, D. Borchardt, P.Y. Feng, Self-doped Ti^{3+} enhanced photocatalyst for hydrogen production under visible light, J. Am. Chem. Soc. 132 (2010) 11856–11857.

[25] X.T. Wang, Y.M. Li, X. Liu, S.M. Gao, B.B. Huang, Y. Dai, Preparation of Ti^{3+} self-doped TiO_2 nanoparticles and their visible light photocatalytic activity, Chin. J. Catal. 36 (2015) 389–399.

[26] R.R. Fu, S.M. Gao, H. Xu, Q.Y. Wang, Z.Y. Wang, B.B. Huang, Y. Dai, Fabrication of Ti^{3+} self-doped TiO_2(A) nanoparticle/TiO_2(R) nanorod heterojunctions with enhanced visible-light-driven photocatalytic properties, RSC Adv. 4 (2014) 37061–37069.

[27] J. Yang, J.H. Swisher, The phase stability of $Zn_2Ti_3O_8$, Mater. Charact. 37 (1996) 153–159.

[28] G. Krylova, A. Brioude, S. Ababou-Girard, J. Mrazeka, L. Spanhel, Natural superhydrophilicity and photocatalytic properties of sol-gel derived $ZnTiO_3$-ilmenite/r-TiO_2 films, Chem. Phys. 12 (2010) 15101–15110.

[29] T. Ohno, T. Tsubota, M. Toyofukum, R. Inaba, Preparation of S-doped TiO_2 photocatalysts and their photocatalytic activities under visible light, Catal. Lett. 265 (2004) 255–258.

[30] S.H. Szczepankiewicz, J.A. Moss, M.R. Hoffmann, Slow surface charge trapping kinetics on irradiated TiO_2, J. Phys. Chem. B 106 (2002) 2922–2927.

[31] Z.L. Xu, J. Shang, C.M. Liu, C.L. Kang, H.C. Guo, Y.G. Du, The preparation and characterization of TiO_2 ultrafine particles, Mater. Sci. Eng. B 63 (1999) 211–214.

[32] J. Zou, J.C. Gao, Y. Wang, Synthesis of highly active H_2O_2-sensitized sulfated titania nanoparticles with a response to visible light, J. Photochem. Photobiol. A Chem. 202 (2009) 128–135.

[33] G. Liu, X.X. Yan, Z.G. Chen, X.W. Wang, L.Z. Wang, G.Q. Lu, H.M. Cheng, Synthesis of rutile-anatase core-shell structured TiO_2 for photocatalysis, J. Mater. Chem. 19 (2009) 6590–6596.

[34] Y. Zhao, C.Z. Li, X.H. Li, F. Gu, H.L. Du, L.Y. Shi, Zn-doped TiO_2 nanoparticles with high photocatalytic activity synthesized by hydrogen–oxygen diffusion flame, Appl. Catal. B Environ. 79 (2008) 208–215.

[35] Z.K. Zheng, B.B. Huang, X.D. Meng, J.P. Wang, S.Y. Wang, Z.Z. Lou, Z.Y. Wang, X.Y. Qin, X.Y. Zhang, Y. Dai, Metallic zinc-assisted synthesis of Ti^{3+} self-doped TiO_2 with tunable phase composition and visible-light photocatalytic activity, Chem. Commun. 49 (2013) 868–870.

[36] J. Mair, P. Nair, F. Mizukami, Y. Oosawa, T. Okubo, Microstructure and phase transformation behavior of doped nanostructured titania, Mater. Res. Bull. 34 (1999) 1275–1290.

[37] S. Li, G. Ye, G. Chen, Low-temperature preparation and characterization of nanocrystalline anatase TiO_2, J. Phys. Chem. C 113 (2009) 4031–4037.

[38] C.K. Xu, D. Gao, Two-stage hydrothermal growth of long ZnO nanowires for efficient TiO_2 nanotube-based dye-sensitized solar cells, J. Phys. Chem. C 116 (2012) 7236–7241.

[39] S.M. Prokes, J.L. Gole, X. Chen, C. Burda, W.E. Carlos, Defect-related optical behavior in surface modified TiO_2 nanostructures, Adv. Funct. Mater. 15 (2005) 161–167.

[40] J.H. Sun, X.L. Wang, J.Y. Sun, R.X. Sun, S.P. Sun, L.P. Qiao, Photocatalytic degradation and kinetics of Orange G using nano-sized Sn(IV)/TiO_2/AC photocatalyst, J. Mol. Catal. A Chem. 260 (2006) 241–246.

[41] X.F. Yang, H.Y. Cui, Y. Li, J.L. Qin, R.X. Zhang, H. Tang, Fabrication of Ag_3PO_4-graphene composites with highly efficient and stable visible light photocatalytic performance, ACS Catal. 3 (2013) 363–369.

[42] Y. Hu, X.H. Gao, L. Yu, Y.R. Wang, J.Q. Ning, S.J. Xu, X.W. Lou, Carbon-coated CdS petalous nanostructures with enhanced photostability and photocatalytic activity, Angew. Chem. 125 (2013) 5746–5749.

[43] K.M. Parida, L. Mohapatra, N. Baliarsingh, Effect of Co^{2+} substitution in the framework of carbonate intercalated Cu/Cr LDH on structural, electronic, optical, and photocatalytic properties, J. Phys. Chem. C 116 (2012) 22417–22424.

[44] Q.J. Xiang, J.G. Yu, M. Jaroniec, Preparation and enhanced visible-light photocatalytic H_2-production activity of graphene/C_3N_4 composites, J. Phys. Chem. C 115 (2011) 7355–7363.

[45] L.B. Xiong, J.L. Li, B. Yang, Y. Yu, Ti^{3+} in the surface of titanium dioxide: generation, properties and photocatalytic application, J. Nanomater. (2012), http://dx.doi.org/10.1155/2012/831524.

[46] X.D. Jiang, Y.P. Zhang, J. Jiang, R.S. Rong, Y.C. Wang, Y.C. Wu, C.X. Pan, Characterization of oxygen vacancy associates within hydrogenated TiO_2: a positron annihilation study, J. Phys. Chem. C 116 (2012) 22619–22624.

[47] T.B. Li, G. Chen, C. Zhou, Z.Y. Shen, R.C. Jin, J.X. Sun, New photocatalyst BiOCl/BiOI composites with highly enhanced visible light photocatalytic performances, Dalton Trans. 40 (2011) 6751–6758.

[48] J.L. Hu, W.J. Fan, W.Q. Ye, C.J. Huang, X.Q. Qiu, Insights into the photosensitivity activity of BiOCl undervisible light irradiation, Appl. Catal. B Environ. 158–159 (2014) 182–189.

[49] P. Deak, B. Aradi, T. Frauenheim, Band lineup and charge carrier separation in mixed rutile-anatase systems, J. Phys. Chem. C 115 (2011) 3443–3446.

[50] K.H. Reddy, S. Martha, K.M. Parida, Fabrication of novel p-BiOI/n-$ZnTiO_3$ heterojunction for degradation of rhodamine 6G under visible light irradiation, Inorg. Chem. 52 (2013) 6390–6401.

[51] T.J. Athauda, J.G. Neff, L. Sutherlin, U. Butt, R.R. Ozer, Systematic study of the structure–property relationships of branched hierarchical TiO_2/ZnO nanostructures, ACS Appl. Mater. Interfaces 4 (2012) 6917–6926.

[52] S. Murphy, C. Saurel, A. Morrissey, J. Tobin, M. Oelgemöler, K. Nolan, Photocatalytic activity of a porphyrin/TiO_2 composite in the degradation of pharmaceuticals, Appl. Catal. B Environ. 119–120 (2012) 156–165.